Materials Characterization 186 (2022) 111779

Contents lists available at ScienceDirect

Materials Characterization

journal homepage: www.elsevier.com/locate/matchar

# Excellent tensile properties induced by heterogeneous grain structure and dual nanoprecipitates in high entropy alloys

Shuang Qin [a], Muxin Yang [a], Ping Jiang [a], Fuping Yuan [a,b,*], Xiaolei Wu [a,b]

[a] State Key Laboratory of Nonlinear Mechanics, Institute of Mechanics, Chinese Academy of Science, 15 Beisihuan West Road, Beijing 100190, China
[b] School of Engineering Science, University of Chinese Academy of Sciences, 19A Yuquan road, Beijing 100049, China

ARTICLE INFO

*Keywords:*
High-entropy alloys
Heterogeneous structures
Precipitates
Strain hardening
Strengthening
Ductility

ABSTRACT

Both heterogeneous grain structure and dual nanoprecipitates (B2 and $L1_2$) have been designed and obtained in a FCC-based $Al_{0.5}Cr_{0.9}FeNi_{2.5}V_{0.2}$ high entropy alloy (HEA). The volume fraction of B2 phase is nearly unchanged, while the average size and volume fraction for $L1_2$ particles become larger after aging, resulting in a more severe heterogeneity. The aged samples display a better synergy of strength and ductility than the corresponding unaged samples. The aged samples show a transient up-turn strain hardening behavior and a higher hardening rate as compared to the corresponding unaged samples. The hetero-deformation-induced hardening plays a more important role in the aged samples than in the unaged samples, producing higher density of geometrically necessary dislocations for better tensile properties. Orowan-type bowing hardening and shearing hardening mechanisms are observed for B2 and $L1_2$ nano-particles, respectively. The size and interspacing of B2 and $L1_2$ particles are at nanometer scale, which should be very effective on hardening and strengthening by accumulating dislocations at phase interfaces. A theoretical analysis based on dislocation strengthening, grain boundary strengthening, Orowan-type bowing strengthening of B2 nano-particles, shearing strengthening of $L1_2$ nano-particles and strengthening of chemical short-range order has been found to provide well prediction on strength.

## 1. Introduction

High-entropy alloys (HEAs) [1–10] and medium-entropy alloys (MEAs) [11–20] are generally solid-solution alloys consisting of multiple principal elements with nearly equal molar fraction. HEAs and MEAs have attracted extensive research interests due to their excellent mechanical properties and other physical properties [21–24]. For example, single phase FCC FeCrMnCoNi HEA [1–4] and CoCrNi MEA [11–16] have been reported recently to exhibit high tensile ductility and exceptional fracture toughness under room temperature, and even better mechanical properties under cryogenic temperature due to a transition of the dominant deformation mechanism from dislocation behavior to deformation twins [3,11].

Although HEAs and MEAs with coarse grains (CG) have excellent tensile properties compared to the other metals and alloys, the structural applications of them are still limited due to the relatively low yield strength [3,11,12]. The strength of metals and alloys can generally be elevated by increased dislocation density or grain refinement through severe plastic deformation [25,26]. However, such elevation of strength in homogeneous structures is usually accompanied by the loss of ductility [27]. Such strength-ductility dilemma in homogeneous structures can be resolved by tailoring microstructures with heterogeneous structures [28–33]. In heterogeneous structures, deformation incompatibility among different domains with dramatic difference in mechanical properties can induce strain gradients and geometrically necessary dislocations (GNDs) for extra strain hardening [34,35]. For example, stress/strain partitioning, strain gradients and hetero-deformation induced (HDI) hardening have been found to play important roles during the tensile deformation in the CoCrNi MEA with heterogeneous grain structures, resulting in a superior combination of strength and ductility [13–16,18].

Besides cold working and grain refinement, the yield strength of alloys can also be enhanced by second-phase particles [36–39]. The second phases with intermetallic particles were generally considered to be detrimental to the ductility of alloys, due to the local stress-strain concentration and the early crack initiation around the hard

* Corresponding author at: State Key Laboratory of Nonlinear Mechanics, Institute of Mechanics, Chinese Academy of Science, 15 Beisihuan West Road, Beijing 100190, China.
*E-mail addresses:* qinshuang@imech.ac.cn (S. Qin), mxyang@lnm.imech.ac.cn (M. Yang), jping@imech.ac.cn (P. Jiang), fpyuan@lnm.imech.ac.cn (F. Yuan), xlwu@imech.ac.cn (X. Wu).

https://doi.org/10.1016/j.matchar.2022.111779
Received 26 September 2021; Received in revised form 29 December 2021; Accepted 2 February 2022
Available online 7 February 2022

precipitates [38,39]. Thus, during the early stage of the development of HEAs and MEAs, the single solid-solution phase without any intermetallic particles has been considered preferentially [1–3]. While, HEAs with secondary phases have also been reported recently [5,40–43]. These second phases with intermetallic particles are generally the ordered B2 phase and $L1_2$ phase. In these studies [43–54], the type, shape, size, volume fraction and distribution of precipitation phases have been properly controlled and tailored for obtaining high strength while retaining sufficient ductility.

Coherent nanoprecipitates have been proven to be an effective strategy to achieve superior tensile properties in alloys due to the minimal lattice misfit and the enhanced strain hardening by accumulating dislocations around coherent nanoprecipitates. In conventional alloys, the coherent ordered $L1_2$ phases in FCC matrix have been considered as one of important strengthening and toughening mechanisms in FCC-based alloys [38,41,55,56], and this strategy in microstructure design has also been found to be effective for resolving the strength-ductility trade-off in HEAs [44,49,57–62]. Besides minimizing the misfit strain for preventing stress concentration at phase interfaces, these coherent nanoprecipitates can also provide precipitation strengthening/hardening to achieve better tensile properties in HEAs and MEAs.

Enlighted by the benefits of heterogeneous grain structures and nanoprecipitates, one can image that better mechanical properties could be obtained by architecting a complex heterogeneous microstructure with both heterogeneous grain structures and nanoprecipitates. While, only complex heterogeneous microstructures with heterogeneous grain structures and one type of nanoprecipitate were considered in previous research. The deformation behaviors and the strain hardening/strengthening mechanisms for HEAs with heterogeneous grain structures and dual nanoprecipitates (B2 and $L1_2$) have not been explored yet. In this regard, a non-equiatomic HEA ($Al_{0.5}Cr_{0.9}FeNi_{2.5}V_{0.2}$) with a high Ni concentration of ~50% and a high Ni/Al ratio of ~5 has been selected as a model system, and the samples with both heterogeneous grain structures and dual nanoprecipitates (B2 and $L1_2$) have been designed and fabricated by cold rolling followed by different heat treatments (partial-recrystallized annealing and aging). Then, the effects of heterogeneous grain structures and dual nanoprecipitates on the tensile behaviors, and the corresponding strain hardening/strengthening mechanisms have been revealed.

## 2. Materials and experimental techniques

The $Al_{0.5}Cr_{0.9}FeNi_{2.5}V_{0.2}$ (in molar ratio) HEA was first prepared by arc-melting under a high-purity argon atmosphere, and then cast into ingots, the ingots were re-melted at least four times to insure the chemical homogeneity. The non-equiatomic system $Al_{0.5}Cr_{0.9}FeNi_{2.5}V_{0.2}$ was designed to generate a near-equiatomic FCC matrix with high content $L1_2$ phase by increasing the Ni/Al ratio, moreover, about 4% V (in at.%) was added to stabilize and strengthen $L1_2$ phase [60]. The as-casted ingots were hot-forged into plates with a thickness of about 8 mm at a starting temperature of 1100 °C. The hot-forged plates were then homogenized at 1200 °C for 24 h in a vacuum environment followed by water quenching, and subsequently were cold-rolled at room temperature with a total thickness reduction of 85%. The as-rolled samples were annealed first at 825, 835, 850, 875, 900, 950 °C for 1 h, or at 1000, 1050, 1100, 1150 °C for 20 min, or at 1200 °C for 2 h followed by water quenching (these samples are named as AN825, AN835, …), and then the annealed samples are aged at 600 °C or 700 °C for 1 h followed by water quenching (these samples are named as AN850_AG600, AN850_AG700, …).

The specimens for quasi-static tensile testing have a plated dog-bone shape, and the gauge section has dimensions of $18 \times 2.5 \times 1.2$ mm$^3$. An Instron 5565 testing machine has been used to conduct the quasi-static uniaxial tensile tests and load-unload-reload (LUR) tests at a strain rate of $5 \times 10^{-4}$ /s and at room temperature under displacement control. The data repeatability has been checked by conducting three tests for each specimen. The tensile direction was designed to be parallel to the rolling direction. During LUR tests, the specimens were first stretched to various pre-determined strains at a strain rate of $5 \times 10^{-4}$ /s, then the specimens were unloaded to 20 N at the unloading rate of 200 N/min under the stress-control mode, followed by reloading at a strain rate of $5 \times 10^{-4}$ /s. The displacement and strain were accurately measured and controlled by an extensometer during both tensile and LUR tests.

Prior to and after tensile testing, X-ray diffraction (XRD), energy disperse spectroscopy (EDS), electron back-scattered diffraction (EBSD), transmission electron microscopy (TEM) and high-resolution electron microscopy (HREM) were used to characterize the microstructures. The surfaces for EBSD were first grinded by sandpapers, and then polished by a 0.05 μm $SiO_2$ aqueous suspension. Thin foils with dimensions of $10 \times 4 \times 0.3$ mm$^3$ were mechanically polished down to about 50 μm thickness using sandpapers, and then thin disks with a diameter of 3 mm were punched by the perforating machine, followed by a twin-jet polishing using a solution of 5% perchloric acid and 95% ethanol at −30 °C and 30 V for TEM observations. A minimum scanning step of 25 nm was used for EBSD acquisition. Grain boundaries (GBs) were defined by misorientation larger than 15 degrees. Kernel average misorientation (KAM) was calculated against the first nearest neighbor ignoring the misorientation larger than 3 degrees.

## 3. Results and discussions

### 3.1. Microstructure characterization prior to tensile testing

In order to identify the phases and the corresponding volume fractions for various phases prior to tensile testing, the XRD spectra for the samples annealed at varying temperatures (referred as unaged samples) and for the samples after aging at 600 °C (referred as aged samples) are shown in Fig. 1a. Since the $L1_2$ precipitates are coherent with the FCC matrix, each of the FCC diffraction peak is actually an overlap of those two phases. Specifically, in this work, the (311) fundamental peaks are used to differentiate the contributions of the FCC and $L1_2$ phases. Fig. 1b displays the close-up view of the overlapped (311) asymmetric peak of FCC phase and $L1_2$ phase for the typical sample. Peak fitting using Gauss function has been applied to the curve, the deconvoluted high-intensity red peak represents the $L1_2$ phase while the relatively low-intensity peak with green color is for the FCC phase. The integrated peak area can be used to estimate the relative volume fraction of each phase [63]. Hence, the relative volume fractions of various phases (FCC, B2 and $L1_2$) for three unaged samples and three corresponding aged samples are given in Fig. 1c. It is observed that the volume fraction of B2 phase decreases with increasing annealing temperature, and B2 phase disappears after annealing at 1200 °C. It is also interesting to note that the volume fraction of B2 phase is nearly unchanged, while the volume fraction of $L1_2$ phase dramatically increases after aging at 600 °C as compared to the corresponding unaged samples.

The EBSD observations for various samples prior to tensile testing are shown in Fig. 2. The inverse pole figures (IPF) for the unaged samples are shown in Fig. 2a, b and c, respectively. The IPF for the corresponding aged samples are displayed in Fig. 2d, e and f, respectively. In Fig. 2a and d, only the distributions of recrystallized CGs are shown by blacking out the area for ultrafine grains (UFGs). Thus, the samples of AN850 and AN850_AG600 clearly show a heterogeneous grain structure consisting of both UFGs and CGs, and the average grain size of recrystallized CGs for these two samples is about 1.3 μm. The corresponding phase maps for the recrystallized CG area are also displayed in the insets of Fig. 2a and d, in which the red color represents the BCC phase (B2) and the yellow color is for the FCC phase (FCC matrix and $L1_2$). It is clearly indicated that B2 particle is much more likely to precipitate at both GBs and triple junctions of FCC grains, instead of their interiors. Based on these two phase maps, the area fraction of B2 phase for these two samples is about 17% and 13% respectively, which is consistent with the results from the XRD measurements (Fig. 1). For the samples of AN1000 and

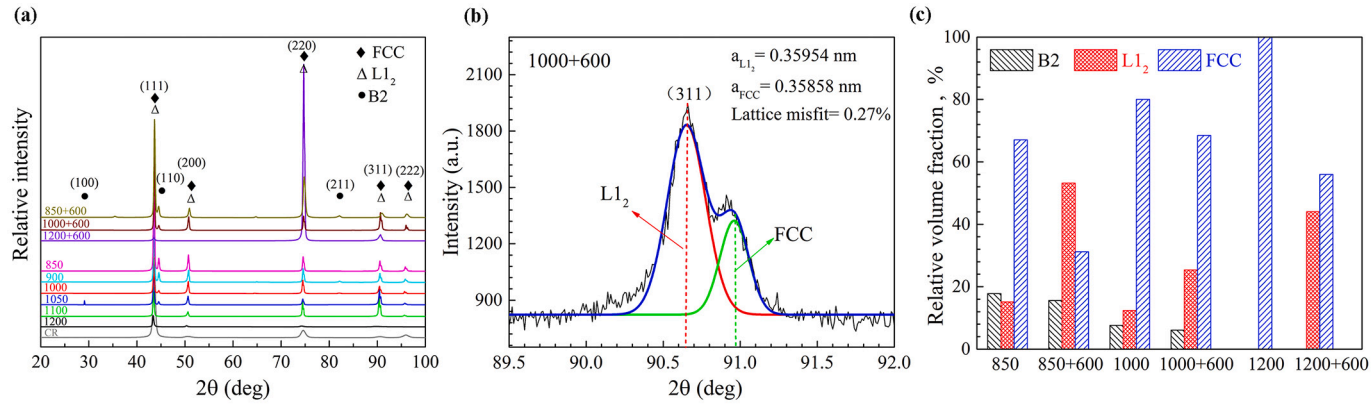


**Fig. 1.** Phase measurements by XRD for various samples. (a) The XRD spectra for various samples. (b) The overlapped (311) asymmetric peaks of FCC phase and $L1_2$ phase for the AN1000 sample. (c) The relative volume fractions of various phases (FCC, B2 and $L1_2$) for three unaged samples and three corresponding aged samples.

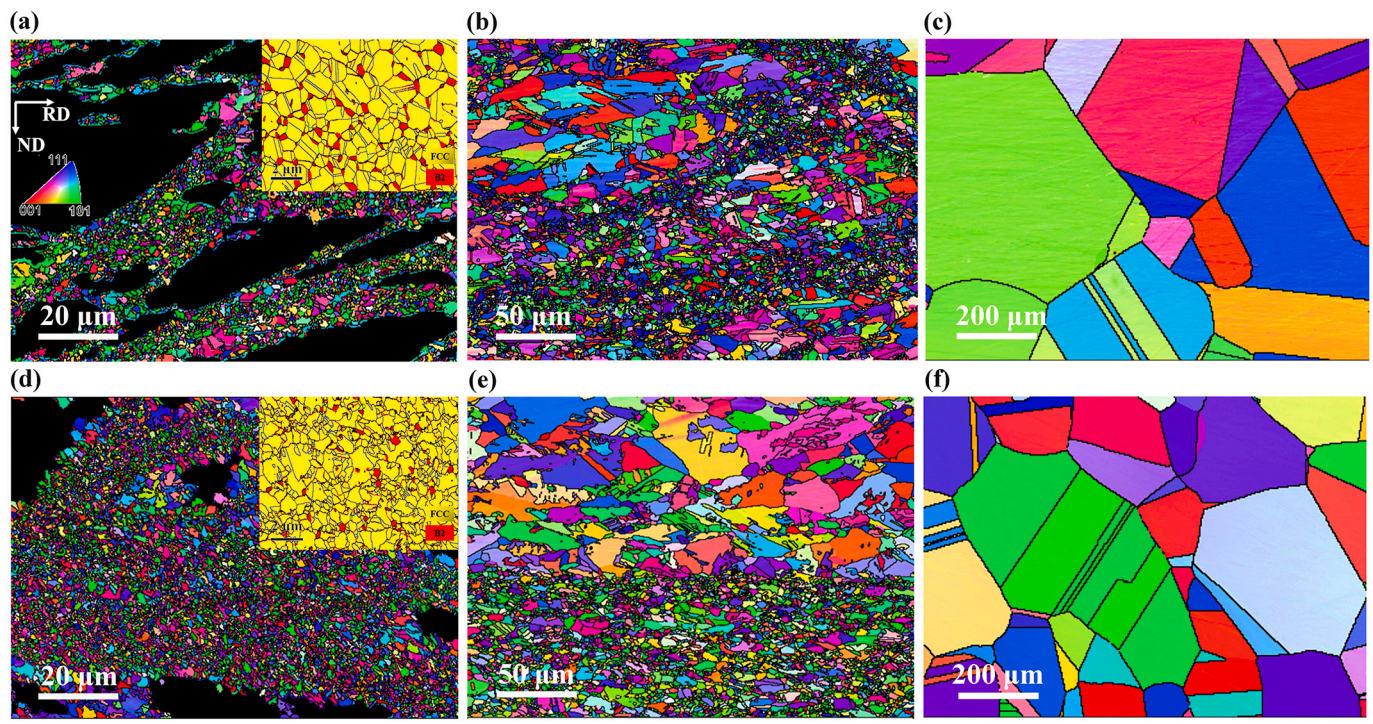


**Fig. 2.** EBSD observations for various samples prior to tensile testing. IPF images for the unaged samples: (a) the AN850 sample; (b) the AN1000 sample; (c) the AN1200 sample. IPF images for the aged samples: (d) the AN850_AG600 sample; (e) the AN1000_AG600 sample; (f) the AN1200_AG600 sample.

AN1000_AG600, the whole area is observed to be fully recrystallized while the microstructures still clearly show a heterogeneous grain structure. In these two samples, the average grain size for the big grains is over 10 μm, while the average grain size for the small grains is about 3 μm. The samples of AN1200 and AN1200_AG600 show a relatively homogeneous structure, and the average grain sizes for these two samples are about 412.3 and 287.9 μm, respectively. A few of annealing twins can also be observed in these two samples.

TEM images for the sample of AN850 are displayed in Fig. 3. In Fig. 3a, both recrystallized CG area and UFG area can be identified, with a clear boundary for these two areas. Fig. 3b shows the close-up view for the un-recrystallized UFG area, B2 particles can be found in this area and be identified by the selected area diffraction (SAD) pattern, and the average size of B2 particles is at sub-micron level. Moreover, high density of dislocations is also observed in this un-recrystallized UFG area, which is in sharp contrast with the clear interior for the recrystallized CG area. In the close-up view for the recrystallized CG area (Fig. 3c), B2 particle can also be clearly identified by the selected area diffraction (SAD) pattern. It is shown that the grains for the recrystallized CG area are nearly free of dislocations due to annealing at 850 °C. Moreover, annealing twins are seen in the FCC CG grains. The B2 particles are also observed to be mostly at sub-micron level. The EDS mapping for an area with a B2 particle is shown in Fig. 3d, in which the element distributions along the marked yellow line are also given. As indicated, Al and Ni elements are enriched in the B2 particle. Previous research [60] has also indicated that the Ni element is highly enriched (about 63%) and the Al element is slightly enriched in the $L1_2$ phase.

Bright-field and Dark-field TEM images for characterizing the size, the interspacing and the relative volume fraction of $L1_2$ phase in the FCC matrix for the samples of AN850 and AN850_AG600 are shown in Fig. 4. Fig. 4a and c display the bright-field TEM images for the samples of AN850 and AN850_AG600, respectively. In Fig. 4a and c, both the FCC phase and the $L1_2$ phase can be identified by SAD patterns in the insets. The Dark-field TEM images for the samples of AN850 and AN850_AG600

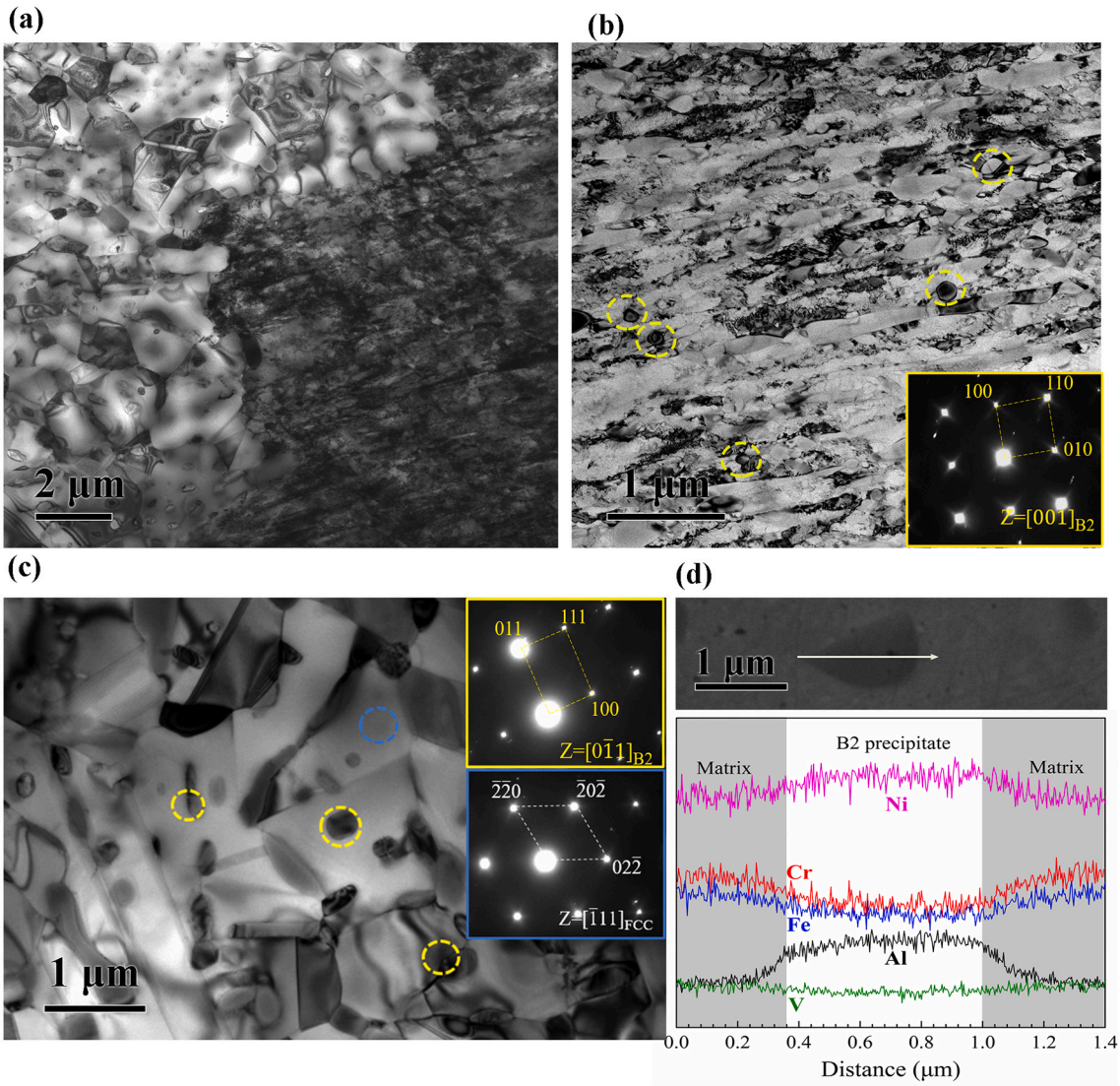


**Fig. 3.** (a) Bright-field TEM image for the AN850 sample prior to tensile testing. (b) Close-up view for the un-recrystallized UFG area in the AN850 sample. (c) Close-up view for the recrystallized CG area in the AN850 sample. (d) EDS mapping for an area with a B2 particle and the element distributions along the marked white line.

are displayed in Fig. 4b and d respectively, in which bright points represent the $L1_2$ particles. The volume fraction of $L1_2$ phase was determined by XRD measurements, and was confirmed by numerous dark-field TEM images. Based on the information for volume fraction, the interspacing and the size of $L1_2$ particles were determined by numerous HRTEM images (Fig. 5). The average size of $L1_2$ particles is estimated to be about 8.5 and 18.4 nm, the average interspacing of $L1_2$ particles is estimated to be about 12.5 and 3.1 nm, and the relative volume fraction of $L1_2$ particles in the FCC matrix is estimated to be about 15% and 55% for the samples of AN850 and AN850_AG600, respectively. It is clearly indicated that the average size becomes larger, the interspacing becomes smaller and the relative volume fraction becomes higher for $L1_2$ particles after aging at 600 °C. Thus, both samples of AN850 and AN850_AG600 have dual heterogeneous structures, but the heterogeneity becomes more severe after aging.

The HREM images and the corresponding images after fast Fourier transform (FFT) and inverse FFT for characterizing the size, the shape and the interspacing of $L1_2$ phase in more details for the samples of AN850 and AN850_AG600 are shown in Fig. 5. Fig. 5a and b show the HREM images for the samples of AN850 and AN850_AG600 respectively, in which the corresponding images of the marked rectangle areas after FFT and inverse FFT are also displayed. In Fig. 5a and b, the FFT images with electron beams closely parallel to the [001] zone axis and the [001] zone axis for the marked rectangle areas clearly indicate that these two nano-domains represent the FCC matrix and the $L1_2$ phase respectively, which are consistent with the atomic packing rules for the corresponding images after FFT and inverse FFT. The large-area images after FFT and inverse FFT for the samples of AN850 and AN850_AG600 are displayed in Fig. 5c and d respectively, in which the $L1_2$ nano-particles are marked and circled by yellow lines. It is clearly indicated that the average size and the relative volume fraction increase, while the average interspacing decreases for the $L1_2$ nano-particles after aging at 600 °C.

### 3.2. Tensile properties and HDI hardening

In order to illustrate the aging effect on the tensile properties, a series of tensile tests have been conducted on the unaged samples and the aged samples. The selected engineering stress-strain curves for the unaged samples and the aged samples are shown in Fig. 6a and b, respectively. In Fig. 6a and b, the yield strength points are marked by circles while the ultimate strength points are indicated by squares. The strain hardening

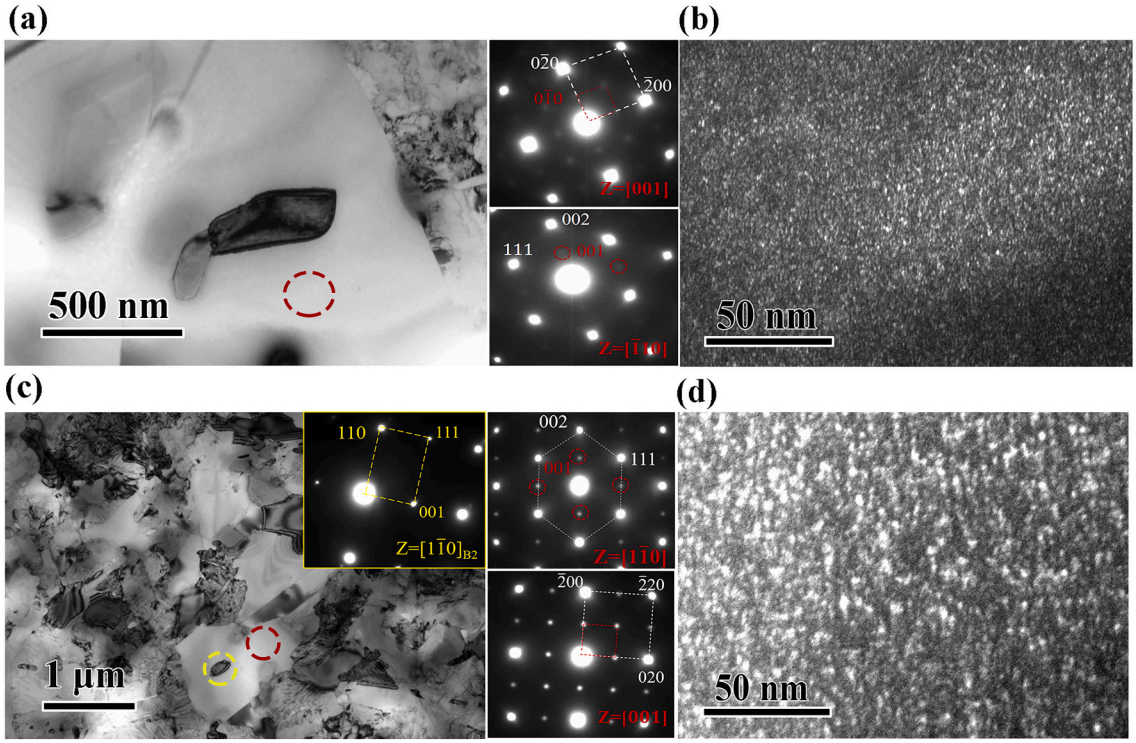


**Fig. 4.** Bright-field (a,c) and dark-field TEM (b,d) images for characterizing the size, the interspacing and the relative volume fraction of $L1_2$ phase in the FCC matrix for the samples of AN850 (a,b) and AN850_AG600 (c,d).

rate $\Theta$ are plotted as a function of true strain for typical samples in Fig. 6c. Two interesting observations should be noted: (i) The hardening rates for the samples after aging display a transient up-turn phenomenon; (ii) The samples after aging are observed to have a higher hardening rate as compared to the corresponding unaged samples. This transient up-turn hardening behavior is typically thought to be induced by the HDI hardening and the heterogeneous elasto-plastic deformation among various domains with dramatic different mechanical properties, resulting in better tensile properties [13]. The higher strain hardening rate for the aged samples can be attributed to the more severe heterogeneity after aging. Then, yield strength is plotted as a function of uniform elongation for the present results in Fig. 6d. It is interesting to note that the samples after aging show a better synergy of strength and ductility than the corresponding unaged samples, and the corresponding deformation and microstructural mechanisms would be revealed next.

It has been reported [13,28,31–35] that excellent tensile properties can be achieved by heterogeneous structures due to the HDI hardening, which can be attributed to the back stress that arises from plastic deformation incompatibility between hard and soft domains. In the dual heterogeneous structure, the smaller UFG grains can be considered as hard domains as compared to the larger CG grains (soft domains), while the B2 and $L1_2$ particles can be considered as even harder domains as compared to the FCC matrix. Thus, the HDI hardening should play an important role in such a dual heterogeneous structure, and the effect of HDI hardening should be more obvious with increasing heterogeneity. In this regard, in order to illustrate and compare the HDI hardening effects on the tensile properties for the aged and unaged samples, the corresponding LUR tests have been conducted and the true stress-strain curves for LUR tests are shown in Fig. 7a.

The typical hysteresis loops at selected unloading strains are displayed in Fig. 7b. The back stress (HDI stress) can be calculated by the average value of the unloading yield stress and the reloading yield stress (marked red and blue circles in Fig. 7b, $\sigma_{HDI} = (\sigma_u + \sigma_r)/2$) from the hysteresis loops of LUR tests, based on the method proposed in our previous paper [34]. Then, $\sigma_{HDI}$ and increment of $\sigma_{HDI}$ after yielding ($\sigma_{HDI} - \sigma_{HDI,\ 0.2}$) are plotted as a function of true strain for these four samples in Fig. 7c. As shown in Fig. 7c, the slopes of the curves for the aged samples are larger than those for the unaged samples. Finally, the HDI hardening rate is plotted as a function of true strain for these four samples in Fig. 7d. It is clearly indicated that the HDI hardening rates for the aged samples are much higher than those for the unaged samples. These observations confirm that the HDI hardening plays a more important role in the aged samples than in the unaged samples, which could be the origin of the better tensile properties in the aged samples.

### 3.3. The microstructural mechanisms for strain hardening

In general, the HDI hardening is accommodated by the GNDs at the boundaries of hard and soft domains [13,34,35,64]. In the present dual heterogeneous structures, GNDs can be produced at the boundaries of UFG grains and CG grains, as well as at the boundaries of different phases (FCC, B2, $L1_2$). The density of GNDs can be estimated by the KAM value using a method based on the strain gradient theory, which was proposed by Gao and Kubin [65,66]: $\rho_{GND} = 2\theta/lb$. Where, $\rho_{GND}$ is the GND density at local points, $\theta$ represents the misorientation at local points, $l$ is the unit length (10 μm in the present study) for the local points, and $b$ is the Burger's vector for the materials (0.254 nm for the current HEA). Thus, the microstructures prior to and after tensile testing for the AN850 and AN850_AG600 samples have been characterized by EBSD, and are displayed in Fig. 8. Fig. 8a and b show the KAM mappings for the sample of AN850 prior to and after tensile testing, respectively. Fig. 8d and e display the KAM mappings for the sample of AN850_AG600 prior to and after tensile testing, respectively. Then, the histogram distributions of GND density prior to and after tensile testing for the sample of AN850 and for the sample of AN850_AG600 are displayed in Fig. 8c and f, respectively. Moreover, the average GND densities prior to and after tensile testing for these two samples are also calculated and indicated in Fig. 8c and f. Thus, the increment of GND density after tensile deformation for the sample of AN850 is estimated to be about $1.064 \times 10^{14}\ m^{-2}$, while that for the sample of AN850_AG600 is observed to be

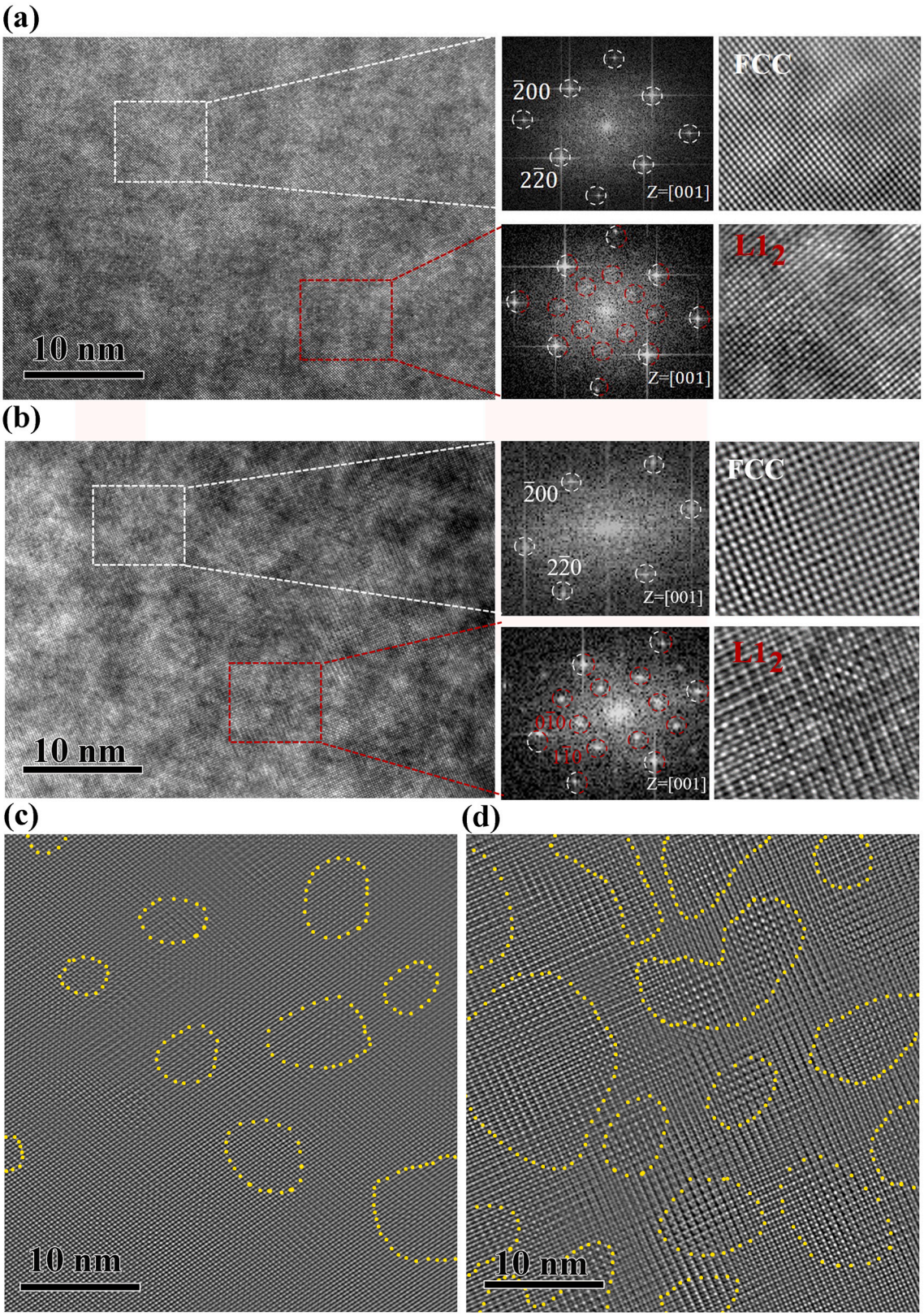


**Fig. 5.** HREM images for characterizing the size, the shape and the interspacing of $L1_2$ phase in the FCC matrix for the samples of (a) AN850 and (b) AN850_AG600. The corresponding images after FFT and inverse FFT for the samples of (c) AN850 and (d) AN850_AG600.

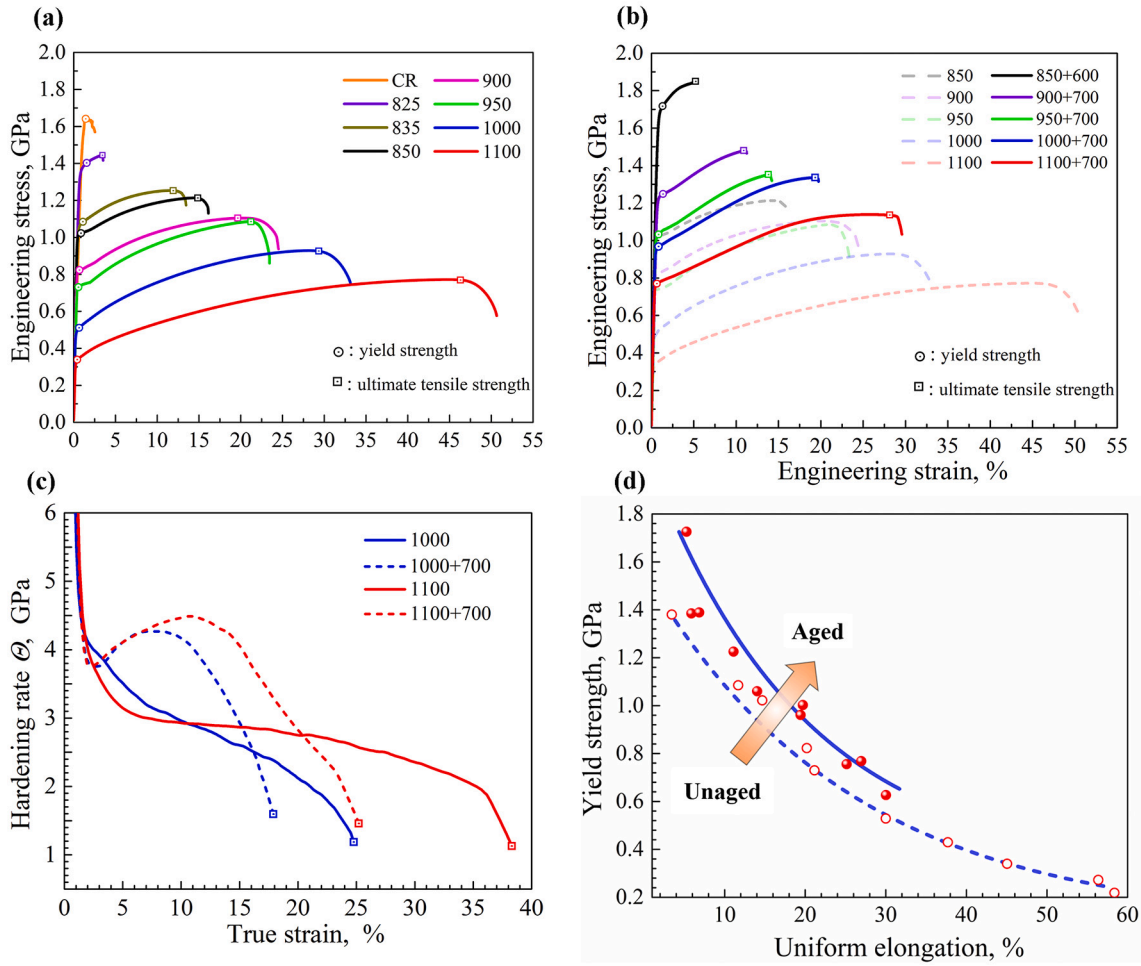


**Fig. 6.** Tensile properties for various samples. (a) Engineering stress-strain curves for the unaged samples. (b) Engineering stress-strain curves for the aged samples (the corresponding curves for the unaged samples are also shown for comparison with faded dash lines). (c) $\Theta$ as a function of true strain for selected samples. (d) Yield strength as a function of uniform elongation for all tested samples in the present study.

much higher (about $2.108 \times 10^{14}$ $m^{-2}$). These results indicated that the strain gradient is more severe in the aged samples as compared to the unaged samples, producing higher density of GNDs, and resulting in stronger HDI hardening for better tensile properties.

TEM observations after tensile testing for the sample of AN850 are displayed in Fig. 9. Extended dislocation pile-ups against two B2 particles can be clearly observed in Fig. 9a, in which leading and trailing partial dislocations are blocked by two B2 nano-particles, leaving SFs between them. Lines of SFs are not clean any more due to the interactions of dislocations from other slip systems with SFs. High density of extended dislocations on two inter-crossing (111) planes are also observed in the FCC matrix, accompanied with formation of Lomer-Cottrell (L-C) locks (Fig. 9a). Dislocation accumulation around the B2 particle is also observed in Fig. 9b, in which high density of bowing full dislocations are blocked and ends of bowing dislocations are pinned by B2 particles. The bulging dislocation lines around B2 nano-particles indicate that dislocations are pushed by the externally applied stress to bow around B2 particles. Hence, the B2 particles act as strengthening/strain hardening agents to block dislocations, resulting in Orowan-type by-pass strengthening/hardening for excellent tensile properties. The size and interspacing of B2 particles is hundreds of nm, which should be very effective on the Orowan-type strengthening/hardening.

It is clearly indicated earlier that the average size is larger, the interspacing is smaller and the relative volume fraction is higher for the $L1_2$ phase in the aged samples. Thus, HREM observations after tensile testing for the sample of AN850_AG600 are displayed in Fig. 10 to show the interaction mechanisms between dislocations and $L1_2$ nano-particles. It is interesting to note that dislocation density is considerably higher near/inside $L1_2$ nano-particles than that away from $L1_2$ nano-particles (Fig. 10a). High density of dislocations are also observed inside $L1_2$ nano-particles in Fig. 10b, indicating in a shearing mechanism of $L1_2$ nano-particles by dislocations. In Fig. 10c, extended dislocations on two inter-crossing (111) planes are observed to be nucleated in the FCC matrix and propagate toward and across the boundary between FCC phase and $L1_2$ phase, leading to formation of L-C lock inside the $L1_2$ nano-particle. Unlike the harder B2 particles, the softer $L1_2$ nano-particles can be sheared by dislocations, resulting in shearing strengthening/hardening for extraordinary tensile properties. The size and interspacing of $L1_2$ nano-particles are both at nanometer scale and the interspacing is even smaller for the aged samples as compared to the unaged samples, which should also be very effective on the shearing strengthening/hardening, resulting in better tensile properties in the aged samples as compared to the unaged samples.

### 3.4. Strengthening mechanisms

In general, the total yield strength traditionally has attributions from several aspects: the solid-solution strengthening $\sigma_{ss}$, the dislocation strengthening $\sigma_{dis}$, the grain-boundary strengthening $\sigma_{gb}$, and the precipitation hardening $\sigma_{ps}$.

Since the dislocation density is very low in the recrystallized grains, dislocation strengthening can be evaluated by the Taylor hardening law:

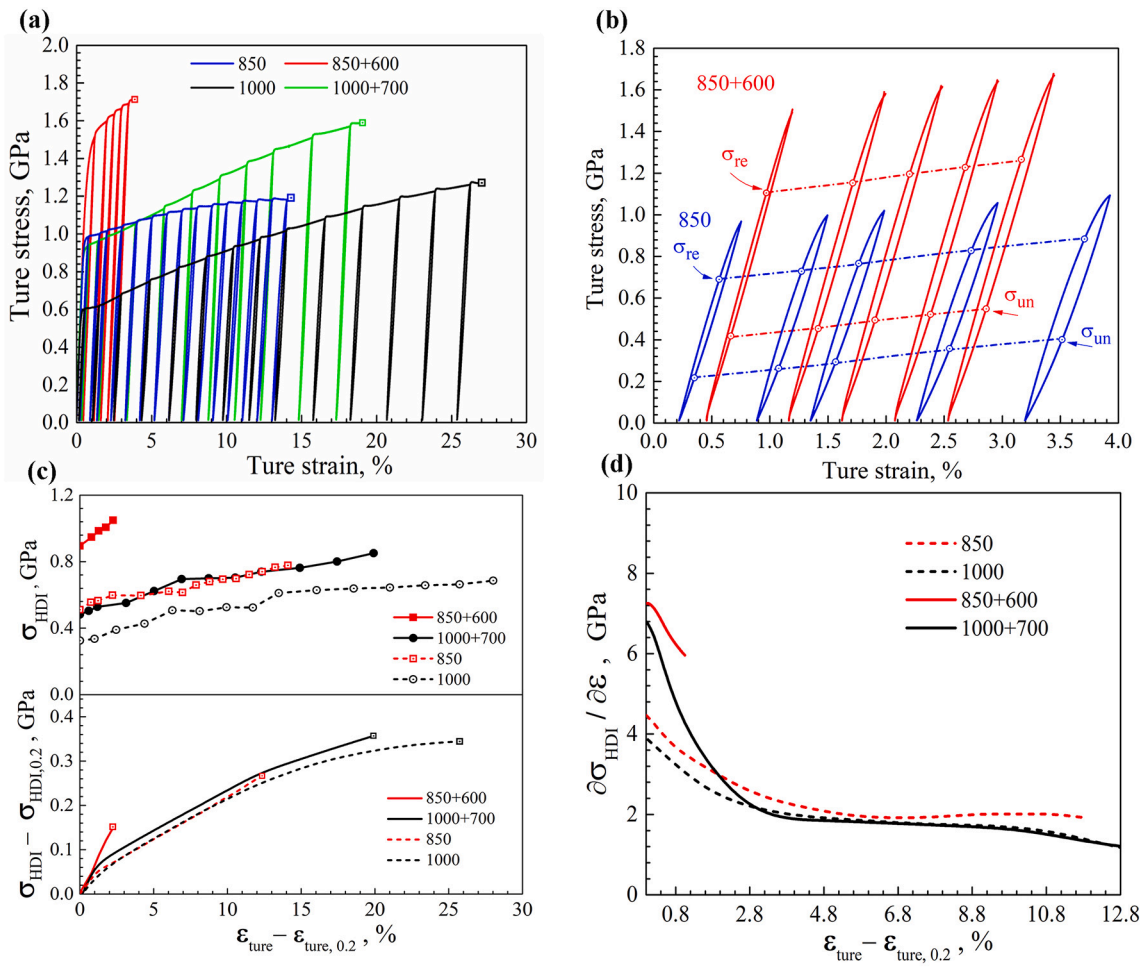


**Fig. 7.** HDI hardening for the typical unaged samples and aged samples. (a) True stress-strain curves for LUR tests. (b) Typical hysteresis loops at selected unloading strains. (c) $\sigma_{HDI}$ and increment of $\sigma_{HDI}$ after yielding ($\sigma_{HDI} - \sigma_{HDI,\ 0.2}$) as a function of true strain. (d) HDI hardening rate as a function of true strain.

$$\sigma_{dis} = f_{URX} M \alpha G b \sqrt{\rho_{dis}} \quad (1)$$

Where $f_{URX}$ is the relative volume fractions of un-recrystallized part (45% for AN850 sample and 30% for AN850_AG600 sample), $\alpha = 0.2$ is a constant, $M = 3.06$ is the Taylor factor for FCC matrix, $G = 77$ GPa is the shear modulus, and $b = 0.254$ nm is the Burgers vector. Moreover, the dislocation density can be estimated by the KAM value. In the present study, the dislocation strengthening effect mainly results from the GNDs since the density of retained statistically stored dislocations is very low due to the recovery upon annealing [41]. Thus, the contributions of dislocation strengthening are calculated as 87 MPa for AN850 sample and 58 MPa for AN850_AG600 sample.

According to the Hall-Petch relation [67], the contribution of grain-boundary strengthening can be estimated by:

$$\sigma_{gb} = K_y \bullet d^{-\frac{1}{2}} \quad (2)$$

where $d$ is the mean grain diameter, and $K_y$ is the coefficient parameter ($K_y = 378.6$ MPa•μm$^{1/2}$ for our alloy [60]). For the heterogeneous grained samples (AN850 and AN850_AG600), the average grain size can be estimated by:

$$d = \overline{d_{RX}} \bullet f_{RX} + \overline{d_{URX}} \bullet f_{URX} \quad (3)$$

where $f_{RX}$ is the relative volume fraction of recrystallized part, $\overline{d_{RX}}$ and $\overline{d_{URX}}$ are the mean grain sizes of recrystallized part and un-recrystallized part. For AN850 sample: $\overline{d_{RX}}$=1.47 μm, $\overline{d_{URX}}$= 0.60 μm, $f_{RX} = 55\%$. For AN850_AG600 sample: $\overline{d_{RX}}$= 1.07 μm, $\overline{d_{URX}}$= 0.60 μm, $f_{RX} = 70\%$. Thus, the contributions of grain-boundary strengthening are 364 and 393 MPa for the AN850 sample and the AN850_AG600 sample, respectively. Additionally, the contribution of solid-solution strengthening $\sigma_{ss}$ can be determined as 196 MPa by the intercept point with the ordinate through linear fitting for the relationship of $\sigma_{gb}$ and $d^{-\frac{1}{2}}$.

In the precipitation-hardened alloys, the interaction between dislocation and precipitate can be classified into two types: bypassing precipitates or shearing precipitates by dislocations. In this work, for the highly ordered, coherent and nanoscale $L1_2$ precipitates, the shearing strengthening is the dominant mechanism. However, for the relatively large and hard B2 particles, the strengthening contribution is mainly determined by the bypassing strengthening (Orowan-type bowing strengthening) effect.

For the estimation of shearing contribution, the modulus mismatch $\sigma_{ms}$, the coherency $\sigma_{cs}$ and the atomic ordering $\sigma_{os}$ between matrix and particle should be simultaneously considered [68–70]. The sum of former two factors estimate the contribution prior to the shearing, and the latter one estimates the contribution during the shearing process. In principle, the larger one determines the final contribution. These contributions can be expressed as:

$$\sigma_{ms} = M \bullet 0.0055 \bullet (\Delta G)^{\frac{3}{2}} \left(\frac{2f}{G}\right)^{\frac{1}{2}} \left(\frac{d}{2b}\right)^{\frac{3m}{2}-1} \quad (4)$$

$$\sigma_{cs} = M \bullet \alpha_{\varepsilon} \bullet (G \bullet \delta)^{\frac{3}{2}} \left(\frac{df}{Gb}\right)^{\frac{1}{2}} \quad (5)$$

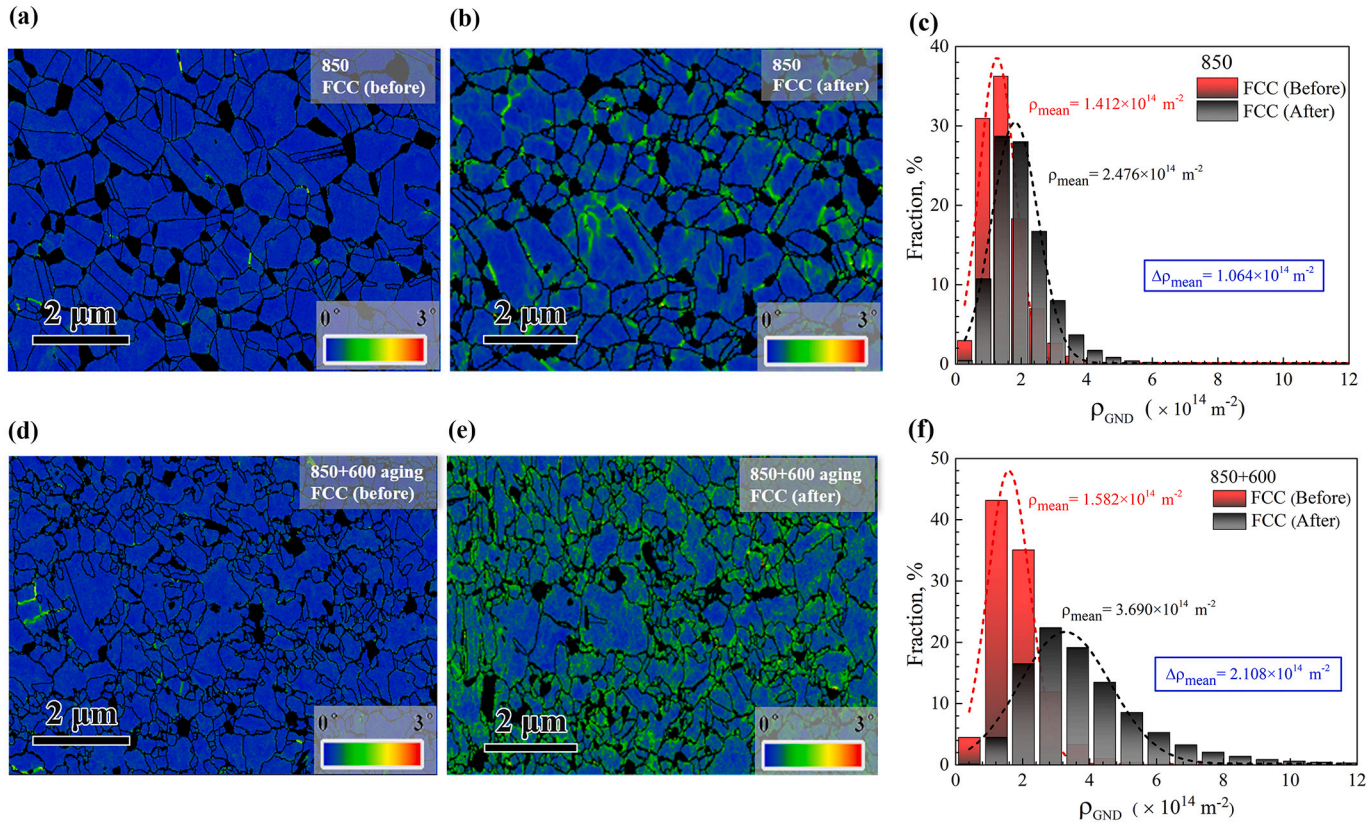


**Fig. 8.** KAM mappings for the sample of AN850 (a) prior to and (b) after tensile testing. KAM mappings for the sample of AN850_AG600 (d) prior to and (e) after tensile testing. Histogram distributions of GND density prior to and after tensile testing (c) for the sample of AN850 and (f) for the sample of AN850_AG600.

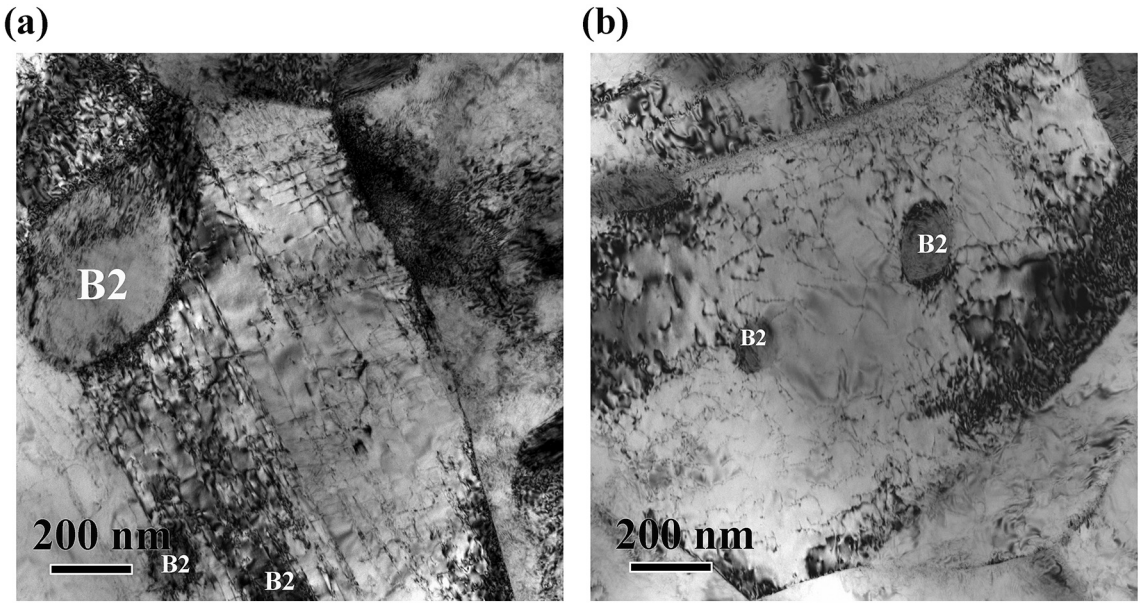


**Fig. 9.** TEM observations after tensile testing for the sample of AN850. (a) Interactions of extended dislocations with B2 particles. (b) Interactions of full dislocations with B2 particles.

$$\sigma_{os} = M \bullet 0.81 \bullet \frac{\gamma_{apb}}{2b}\left(\frac{3\pi f}{8}\right)^{\frac{1}{2}} \quad (6)$$

Where $\Delta G = 4$ GPa is the modulus mismatch between the matrix and precipitates, $f$ is the volume fraction of the ordered $L1_2$ precipitates, $d$ is the average diameter of precipitate, $\alpha_\varepsilon = 2.6$ for FCC structure [71]. $\delta$ is the constrained lattice misfit, the lattice constant can be derived from XRD patterns, $\gamma_{apb} = 0.2$ J/m$^2$ is the antiphase boundary free energy of the $Ni_3Al$ precipitate phase [60]. Consequently, the contributions of shearing precipitation for the AN850 sample are 335 MPa ($\sigma_{ms} + \sigma_{cs} =$ 96 MPa, $\sigma_{os} =$ 335 MPa). Similarly, for the AN850_AG600 sample, the resultant contribution is 791 MPa ($\sigma_{ms} + \sigma_{cs} =$ 563 MPa, $\sigma_{os} =$ 791 MPa).

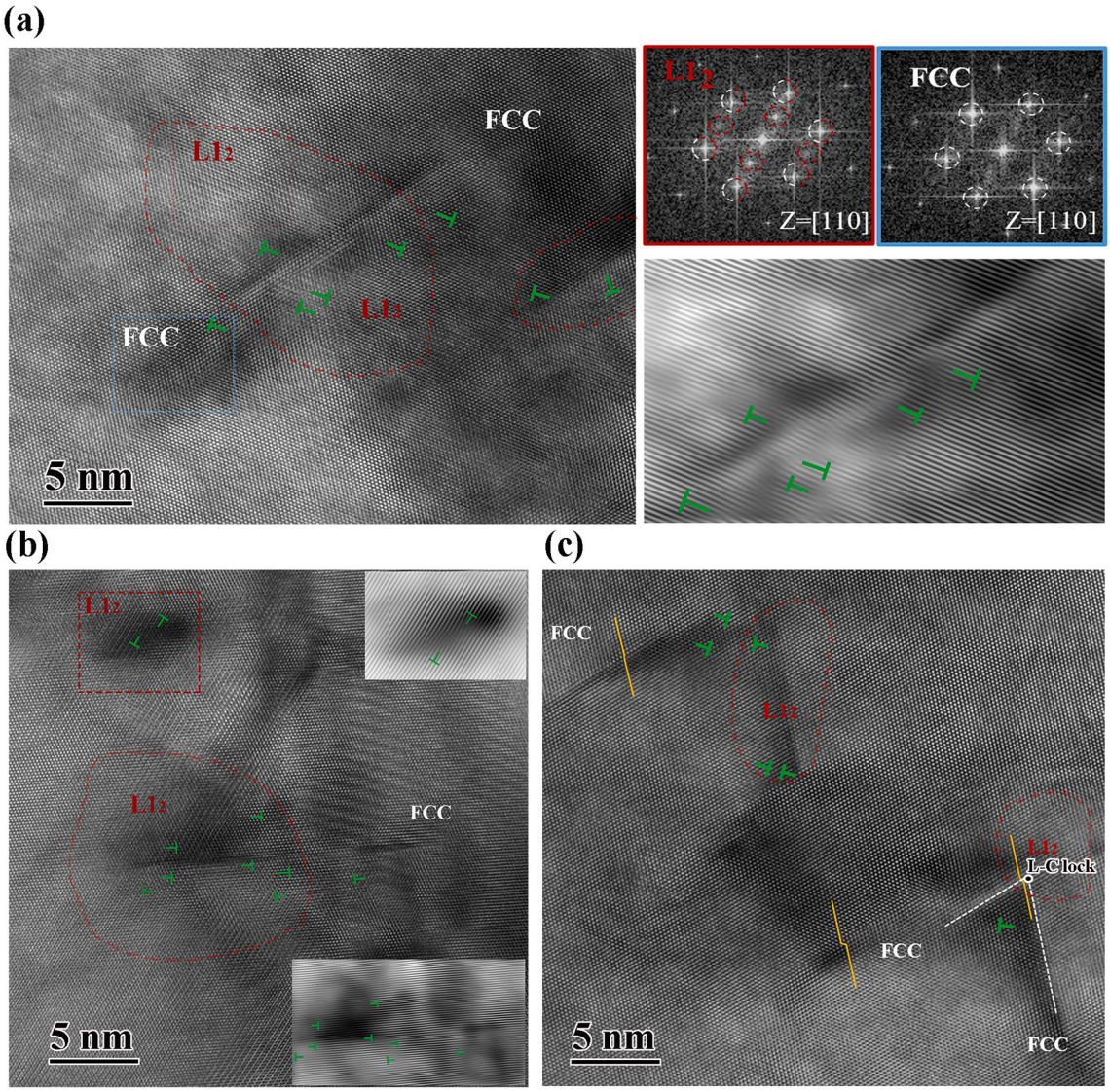


**Fig. 10.** HREM observations after tensile testing for the sample of AN850_AG600. (a) Dislocation accumulation around $L1_2$ nano-particles, in which the FCC phase and the $L1_2$ phase are indicated by the image after FFT and the dislocations (marked by T) can be clearly seen in the corresponding image after FFT and IFFT. (b) Shearing of $L1_2$ nano-particles by dislocations, in which high density of dislocations can be clearly observed inside $L1_2$ nano-particles in the corresponding images after FFT and IFFT. (c) Extended dislocations on two inter-crossing (111) planes across the boundary between FCC phase and $L1_2$ phase, leading to formation of L-C lock inside $L1_2$ phase.

The contribution of Orowan-type strengthening can be written as:

$$\sigma_{\text{bypass}} = \frac{0.4\text{M}Gb}{\pi\sqrt{1-\nu}} \frac{ln\left(\sqrt{\frac{2}{3}} \bullet \frac{d}{b}\right)}{\lambda_{\text{p}}} \tag{7}$$

where $\nu = 0.31$ is the Poisson's ratio and $\lambda_p$ is the average edge-to-edge inter-distance of B2 precipitates [44,72]. Thus, the contributions of bypassing mechanisms for the B2 particles are calculated as 46 MPa for AN850 sample and 65 MPa for AN850_AG600 sample. Obviously, the contribution of by-pass strengthening is relatively low compared to the shearing strengthening, mainly due to the much larger interspacing of B2 particles in both samples.

In summary, the theoretical calculation strength of the AN850 sample and AN850_AG600 sample are estimated as 1028 MPa and 1503 MPa, respectively. A discrepancy is observed between the predicted results and the experimental data, which could be attributed to the other unconsidered strengthening effects, such as extra HDI strengthening and strengthening by chemical short-range order (CSRO) [35,73–78]. The dislocation strengthening is closely related to the existing GNDs prior to tensile testing, according to the Taylor equation. While the yielding process in the heterogeneous structure displays an elasto-plastic transition stage. The load transfer and strain partitioning can produce new GNDs upon tensile loading, resulting in HDI strengthening. CSRO has been found to have strong strengthening effect due to the interactions between dislocations and CSRO domains. In general, the degree of CSRO increases after long-time aging at low temperatures [73,76]. Thus, the aged samples should have a higher degree of CSRO and have a higher strengthening contribution from CSRO, which is consistent with the larger discrepancy between the predicted results and the experimental data for the aged samples, as shown in Fig. 11. The characterization of CSRO and the estimation for the strengthening contribution of CSRO will be studied in the future work.

## 4. Summary and concluding remarks

In the present study, a complex heterogeneous structure with both heterogeneous grain structure and dual nanoprecipitates (B2 and $L1_2$)

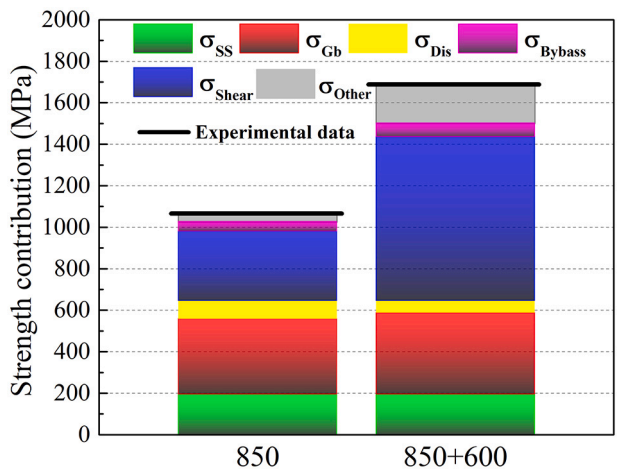


**Fig. 11.** Strength contributions from various mechanisms for the samples of AN850 and AN850_AG600.

has been obtained in a $Al_{0.5}Cr_{0.9}FeNi_{2.5}V_{0.2}$ HEA utilizing cold rolling followed by annealing and aging. Then, the tensile properties and the corresponding deformation mechanisms have been investigated, and the findings are summarized as follows:

(1) The volume fraction of B2 phase is nearly unchanged after aging. While for $L1_2$ particles after aging, it is clearly observed that the average size becomes larger (from 8.5 to 18.4 nm), the interspacing becomes smaller (12.5 to 3.1 nm) and the relative volume fraction (from 15% to 55%) becomes higher, resulting in a more severe heterogeneity.

(2) The aged samples are found to display a better synergy of strength and ductility than the corresponding unaged samples. The aged samples show a transient up-turn strain hardening behavior and a higher hardening rate as compared to the corresponding unaged samples. The HDI hardening rates for the aged samples are observed to be much higher than those for the unaged samples. The HDI hardening plays a more important role in the aged samples than in the unaged samples, which is the origin of the better tensile properties in the aged samples.

(3) The strain gradient during tensile deformation is found to be more severe in the aged samples as compared to the unaged samples, producing higher density of GNDs, and resulting in stronger HDI hardening for better tensile properties. B2 particles are observed to block dislocations for dislocation accumulation, resulting in Orowan-type bowing strengthening/hardening. While, shearing strengthening/hardening mechanism has been observed for $L1_2$ nano-particles. The size and interspacing of $L1_2$ nano-particles are at nanometer scale for the unaged samples, and the interspacing is even smaller for the aged samples as compared to the unaged samples, which should be very effective on hardening and strengthening by accumulating dislocations at phase interfaces.

(4) A theoretical analysis based on dislocation strengthening, GB strengthening, Orowan-type bowing strengthening of B2 particles, shearing strengthening of $L1_2$ nano-particles and strengthening of CSRO has been conducted to predict the strength of the unaged and aged samples, the predicted results are in relatively well agreement with experimental data. The present results should provide insights for achieving extraordinary tensile properties in HEAs by architecting dual heterogeneous structures.

## Data availability

The raw/processed data required to reproduce these findings cannot be shared at this time due to technical or time limitations.

## Declaration of Competing Interest

The authors declare that they have no known competing financial interests or personal relationships that could have appeared to influence the work reported in this paper.

## Acknowledgements

This research was supported by the National Key R&D Program of China [grant number 2017YFA0204402]; the NSFC Basic Science Center Program for “Multiscale Problems in Nonlinear Mechanics” [grant number 11988102], the National Natural Science Foundation of China [grant numbers 11790293, 52192591], the fellowship of China Postdoctoral Science Foundation [grant number 2021M703292], and the Strategic Priority Research Program of the Chinese Academy of Sciences [grant number XDB22040503].

## References

[1] J.W. Yeh, S.K. Chen, S.J. Lin, J.Y. Gan, T.S. Chin, T.T. Shun, C.H. Tsau, S.Y. Chang, Nanostructured high-entropy alloys with multiple principal elements: novel alloy design concepts and outcomes, Adv. Eng. Mater. 6 (2004) 299–303.
[2] B. Cantor, I.T.H. Chang, P. Knight, A.J.B. Vincent, Microstructural development in equiatomic multicomponent alloys, Mater. Sci. Eng. A 375–377 (2004) 213–218.
[3] B. Gludovatz, A. Hohenwarter, D. Catoor, E.H. Chang, E.P. George, R.O. Ritchie, A fracture-resistant high-entropy alloy for cryogenic applications, Science. 345 (2014) 1153–1158.
[4] B. Schuh, F. Mendez-Martin, B. Völker, E.P. George, H. Clemens, R. Pippan, A. Hohenwarter, Mechanical properties, microstructure and thermal stability of a nanocrystalline CoCrFeMnNi high-entropy alloy after severe plastic deformation, Acta Mater. 96 (2015) 258–268.
[5] Z.M. Li, K.G. Pradeep, Y. Deng, D. Raabe, C.C. Tasan, Metastable high-entropy dual-phase alloys overcome the strength–ductility trade-off, Nature. 534 (2016) 227–230.
[6] Z.F. Lei, X.J. Liu, Y. Wu, H. Wang, S.H. Jiang, S.D. Wang, X.D. Hui, Y.D. Wu, B. Gault, P. Kontis, D. Raabe, L. Gu, Q.H. Zhang, H. Chen, H.T. Wang, J.B. Liu, K. An, Q.S. Zeng, T.-G. Nieh, Z.P. Lu, Enhanced strength and ductility in a high-entropy alloy via ordered oxygen complexes, Nature. 563 (2018) 546–550.
[7] M. Wang, Y. Lu, T. Wang, C. Zhang, Z. Cao, T. Li, P.K. Liaw, A novel bulk eutectic high-entropy alloy with outstanding as-cast specific yield strengths at elevated temperatures, Scr. Mater. 204 (2021), 114132.
[8] E.P. George, D. Raabe, R.O. Ritchie, High-entropy alloys, Nat. Rev. Mater. 4 (2019) 515–534.
[9] Y.P. Lu, X.Z. Gao, L. Jiang, Z.N. Chen, T.M. Wang, J.C. Jie, H.J. Kang, Y.B. Zhang, S. Guo, H.H. Ruan, Y.H. Zhao, Z.Q. Cao, T.J. Li, Directly cast bulk eutectic and near-eutectic high entropy alloys with balanced strength and ductility in a wide temperature range, Acta Mater. 124 (2017) 143–150.
[10] Z.L. Yang, M.X. Yang, Y. Ma, L.L. Zhou, W.Q. Cheng, F.P. Yuan, X.L. Wu, Strain rate dependent shear localization and deformation mechanisms in the CrMnFeCoNi high-entropy alloy with various microstructures, Mater. Sci. Eng. A 793 (2020), 139854.
[11] B. Gludovatz, A. Hohenwarter, K.V.S. Thurston, H.B. Bei, Z.G. Wu, E.P. George, R. O. Ritchie, Exceptional damage-tolerance of a medium-entropy alloy CrCoNi at cryogenic temperatures, Nat. Commun. 7 (2016) 10602.
[12] J. Miao, C.E. Slone, T.M. Smith, C. Niu, H. Bei, M. Ghazisaeidi, G.M. Pharr, M. J. Mills, The evolution of the deformation substructure in a Ni-co-Cr equiatomic solid solution alloy, Acta Mater. 132 (2017) 35–48.
[13] M.X. Yang, D.S. Yan, F.P. Yuan, P. Jiang, E. Ma, X.L. Wu, Dynamically reinforced heterogeneous grain structure prolongs ductility in a medium-entropy alloy with gigapascal yield strength, Proc. Natl. Acad. Sci. 115 (2018) 7224–7229.
[14] Y. Ma, F.P. Yuan, M.X. Yang, P. Jiang, E. Ma, X.L. Wu, Dynamic shear deformation of a CrCoNi medium-entropy alloy with heterogeneous grain structures, Acta Mater. 148 (2018) 407–418.
[15] M.X. Yang, L.L. Zhou, C. Wang, P. Jiang, F.P. Yuan, E. Ma, X.L. Wu, High impact toughness of CrCoNi medium-entropy alloy at liquid-helium temperature, Scr. Mater. 172 (2019) 66–71.
[16] X.L. Wu, M.X. Yang, P. Jiang, C. Wang, L.L. Zhou, F.P. Yuan, E. Ma, Deformation nanotwins suppress shear banding during impact test of CrCoNi medium-entropy alloy, Scr. Mater. 178 (2020) 452–456.
[17] S.S. Sohn, A.K. da Silva, Y. Ikeda, F. Körmann, W.J. Lu, W.S. Choi, B. Gault, D. Ponge, J. Neugebauer, D. Raabe, Ultrastrong medium-entropy single-phase alloys designed via severe lattice distortion, Adv. Mater. 31 (2019) 1807142.

[18] C.E. Slone, J. Miao, E.P. George, M.J. Mills, Achieving ultra-high strength and ductility in equiatomic CrCoNi with partially recrystallized microstructures, Acta Mater. 165 (2019) 496–507.
[19] J. Ding, Q. Yu, M. Asta, R.O. Ritchie, Tunable stacking fault energies by tailoring local chemical order in CrCoNi medium-entropy alloys, Proc. Natl. Acad. Sci. U. S. A. 115 (2018) 8919–8924.
[20] Y. Ma, M.X. Yang, F.P. Yuan, X.L. Wu, Deformation induced hcp nano-lamella and its size effect on the strengthening in a CoCrNi medium-entropy alloy, J. Mater. Sci. Technol. 82 (2021) 122–134.
[21] Y. Lu, Y. Dong, H. Jiang, Z. Wang, Z. Cao, S. Guo, T. Wang, T. Li, P.K. Liaw, Promising properties and future trend of eutectic high entropy alloys, Scr. Mater. 187 (2020) 202–209.
[22] M. Wang, H. Cui, Y. Zhao, C. Wang, N. Wei, X. Gao, Q. Song, Enhanced strength and ductility in a spark plasma sintered $CoCrCu_{0.5}NiAl_{0.5}$ high-entropy alloy via a double-step ball milling approach for processing powders, Mater. Sci. Eng. A 762 (2019), 138071.
[23] R. Feng, C. Zhang, M.C. Gao, Z.R. Pei, F. Zhang, Y. Chen, D. Ma, K. An, J. D. Poplawsky, L.Z. Ouyang, Y. Ren, J.A. Hawk, M. Widom, P.K. Liaw, High-throughput design of high-performance lightweight high-entropy alloys, Nat. Commun. 12 (2021) 4329.
[24] C. Zhang, C. Zhu, P. Cao, X. Wang, F. Ye, K. Kaufmann, L. Casalena, B. E. MacDonald, X. Pan, K. Vecchio, E.J. Lavernia, Aged metastable high-entropy alloys with heterogeneous lamella structure for superior strength-ductility synergy, Acta Mater. 199 (2020) 602–612.
[25] R.Z. Valiev, I.V. Alexandrov, Y.T. Zhu, T.C. Lowe, Paradox of strength and ductility in metals processed Bysevere plastic deformation, J. Mater. Res. 17 (2002) 5–8.
[26] M.A. Meyers, A. Mishra, D.J. Benson, Mechanical properties of nanocrystalline materials, Prog. Mater. Sci. 51 (2006) 427–556.
[27] Y.T. Zhu, X.Z. Liao, Retaining ductility, Nat. Mater. 3 (2004) 351–352.
[28] X.L. Wu, Y.T. Zhu, Heterogeneous materials: a new class of materials with unprecedented mechanical properties, Mater. Res. Lett. 5 (2017) 527–532.
[29] T.H. Fang, W.L. Li, N.R. Tao, K. Lu, Revealing extraordinary intrinsic tensile plasticity in gradient nano-grained copper, Science. 331 (2011) 1587–1590.
[30] X.L. Wu, P. Jiang, L. Chen, F.P. Yuan, Y.T. Zhu, Extraordinary strain hardening by gradient structure, Proc. Natl. Acad. Sci. 111 (2014) 7197–7201.
[31] X.L. Wu, M.X. Yang, F.P. Yuan, G.L. Wu, Y.J. Wei, X.W. Huang, Y.T. Zhu, Heterogeneous lamella structure unites ultrafine-grain strength with coarse-grain ductility, Proc. Natl. Acad. Sci. U. S. A. 112 (2015) 14501–14505.
[32] C.D. Dai, Y. Fu, Y. Pan, Y.P. Yin, C.W. Du, Z.Y. Liu, Microstructure and mechanical properties of FeCoCrNiMo0.1 high-entropy alloy with various annealing treatments, Mater. Charact. 179 (2021), 111313.
[33] H. Wang, X.H. Chen, H.L. Zhou, Y. Jiang, P. Liu, Static recrystallized annealing treatment-induced strength-ductility trade-off in cold-rolled Co36Fe36Cr18Ni10 multi-principal alloy, Mater. Charact. 179 (2021), 111254.
[34] M.X. Yang, Y. Pan, F.P. Yuan, Y.T. Zhu, X.L. Wu, Back stress strengthening and strain hardening in gradient structure, Mater. Res. Lett. 4 (2016) 145–151.
[35] Y.T. Zhu, X.L. Wu, Perspective on hetero-deformation induced (HDI) hardening and back stress, Mater. Res. Lett. 7 (2019) 393–398.
[36] P.V. Liddicoat, X.Z. Liao, Y.H. Zhao, Y.T. Zhu, M.Y. Murashkin, E.J. Lavernia, R. Z. Valiev, S.P. Ringer, Nanostructural hierarchy increases the strength of aluminium alloys, Nat. Commun. 1 (2010) 63.
[37] G. Liu, G.J. Zhang, F. Jiang, X.D. Ding, Y.J. Sun, J. Sun, E. Ma, Nanostructured high-strength molybdenum alloys with unprecedented tensile ductility, Nat. Mater. 12 (2013) 344–350.
[38] S.H. Kim, H. Kim, N.J. Kim, Brittle intermetallic compound makes ultrastrong low-density steel with large ductility, Nature. 518 (2015) 77–79.
[39] I. Gutierrez-Urrutia, D. Raabe, Influence of Al content and precipitation state on the mechanical behavior of austenitic high-Mn low-density steels, Scr. Mater. 68 (2013) 343–347.
[40] Y.H. Jo, W.M. Choi, D.G. Kim, A. Zargaran, K. Lee, H. Sung, S.S. Sohn, H.S. Kim, B. J. Lee, S. Lee, Utilization of brittle σ phase for strengthening and strain hardening in ductile VCrFeNi high-entropy alloy, Mater. Sci. Eng. A 743 (2019) 665–674.
[41] Z.W. Wang, W.J. Lu, H. Zhao, C.H. Liebscher, J.Y. He, D. Ponge, D. Raabe, Z.M. Li, Ultrastrong lightweight compositionally complex steels via dual-nanoprecipitation, Sci. Adv. 6 (2020) eaba9543.
[42] H. Jiang, K.M. Han, X.X. Gao, Y.P. Lu, Z.Q. Cao, M.C. Gao, J.A. Hawk, T.J. Li, A new strategy to design eutectic high-entropy alloys using simple mixture method, Mater. Des. 142 (2018) 101–105.
[43] Y. Yang, T.Y. Chen, L.Z. Tan, J.D. Poplawsky, K. An, Y.L. Wang, G.D. Samolyuk, K. Littrell, A.R. Lupini, A. Borisevich, E.P. George, Bifunctional nanoprecipitates strengthen and ductilize a medium-entropy alloy, Nature. 595 (2021) 245–249.
[44] T. Yang, Y.L. Zhao, Y. Tong, Z.B. Jiao, J. Wei, J.X. Cai, X.D. Han, D. Chen, A. Hu, J. J. Kai, K. Lu, Y. Liu, C.T. Liu, Multicomponent intermetallic nanoparticles and superb mechanical behaviors of complex alloys, Science. 362 (2018) 933.
[45] K.S. Ming, X.F. Bi, J. Wang, Realizing strength-ductility combination of coarse-grained Al0.2Co1.5CrFeNi1.5Ti0.3 alloy via nano-sized, coherent precipitates, Int. J. Plast. 100 (2018) 177–191.
[46] B. Gwalani, V. Soni, D. Choudhuri, M. Lee, J.Y. Hwang, S.J. Nam, H. Ryu, S. H. Hong, R. Banerjee, Stability of ordered L12 and B2 precipitates in face centered cubic based high entropy alloys - Al0.3CoFeCrNi and Al0.3CuFeCrNi2, Scr. Mater. 123 (2016) 130–134.
[47] Y.Y. Zhao, H.W. Chen, Z.P. Lu, T.G. Nieh, Thermal stability and coarsening of coherent particles in a precipitation-hardened (NiCoFeCr)94Ti2Al4 high-entropy alloy, Acta Mater. 147 (2018) 184–194.
[48] Z.G. Wang, W. Zhou, L.M. Fu, J.F. Wang, R.C. Luo, X.C. Han, B. Chen, X.D. Wang, Effect of coherent L12 nanoprecipitates on the tensile behavior of a fcc-based high-entropy alloy, Mater. Sci. Eng. A 696 (2017) 503–510.
[49] T. Yang, Y.L. Zhao, W.H. Liu, J.J. Kai, C. Liu, L12-strengthened high-entropy alloys for advanced structural applications, J. Mater. Res. 33 (2018) 2983–2997.
[50] J.C. Rao, H.Y. Diao, V. Ocelík, D. Vainchtein, C. Zhang, C. Kuo, Z. Tang, W. Guo, J. D. Poplawsky, Y. Zhou, P.K. Liaw, J.Th.M. De Hosson, Secondary phases in $Al_xCoCrFeNi$ high-entropy alloys: An in-situ TEM heating study and thermodynamic appraisal, Acta Mater. 131 (2017) 206–220.
[51] Y.L. Zhao, T. Yang, Y. Tong, J. Wang, J.H. Luan, Z.B. Jiao, D. Chen, Y. Yang, A. Hu, C.T. Liu, J.-J. Kai, Heterogeneous precipitation behavior and stacking-fault-mediated deformation in a CoCrNi-based medium-entropy alloy, Acta Mater. 138 (2017) 72–82.
[52] L. Fan, T. Yang, Y. Zhao, J. Luan, G. Zhou, H. Wang, Z. Jiao, C.-T. Liu, Ultrahigh strength and ductility in newly developed materials with coherent nanolamellar architectures, Nat. Commun. 11 (2020) 6240.
[53] M.L. Wang, H.Z. Cui, Y.Q. Zhao, C.M. Wang, N. Wei, Y. Zhao, X. Zhang, Q. Song, A simple strategy for fabrication of an FCC-based complex concentrated alloy coating with hierarchical nanoprecipitates and enhanced mechanical properties, Mater. Des. 180 (2019), 107893.
[54] L. Han, Z.Y. Rao, I.R. Souza Filho, F. Maccari, Y. Wei, G. Wu, A. Ahmadian, X. Y. Zhou, O. Gutfleisch, D. Ponge, D. Raabe, Z.M. Li, Ultrastrong and ductile soft magnetic high-entropy alloys via coherent ordered nanoprecipitates, Adv. Mater. 33 (2021) 2102139.
[55] S.H. Jiang, H. Wang, Y. Wu, X.J. Liu, H.H. Chen, M.J. Yao, B. Gault, D. Ponge, D. Raabe, A. Hirata, M.W. Chen, Y.D. Wang, Z.P. Lu, Ultrastrong steel via minimal lattice misfit and high-density nanoprecipitation, Nature. 544 (2017) 460–464.
[56] Z.B. Jiao, J.H. Luan, M.K. Miller, C.T. Liu, Precipitation mechanism and mechanical properties of an ultra-high strength steel hardened by nanoscale NiAl and cu particles, Acta Mater. 97 (2015) 58–67.
[57] X.H. Du, W.P. Li, H.T. Chang, T. Yang, G.S. Duan, B.L. Wu, J.C. Huang, F.R. Chen, C.T. Liu, W.S. Chuang, Y. Lu, M.L. Sui, E.W. Huang, Dual heterogeneous structures lead to ultrahigh strength and uniform ductility in a co-Cr-Ni medium-entropy alloy, Nat. Commun. 11 (2020) 2390.
[58] Y. Tong, D. Chen, B. Han, J. Wang, R. Feng, T. Yang, C. Zhao, Y.L. Zhao, W. Guo, Y. Shimizu, C.T. Liu, P.K. Liaw, K. Inoue, Y. Nagai, A. Hu, J.J. Kai, Outstanding tensile properties of a precipitation-strengthened $FeCoNiCrTi_{0.2}$ high-entropy alloy at room and cryogenic temperatures, Acta Mater. 165 (2019) 228–240.
[59] T. Yang, Y.L. Zhao, J.H. Luan, B. Han, J. Wei, J.J. Kai, C.T. Liu, Nanoparticles-strengthened high-entropy alloys for cryogenic applications showing an exceptional strength-ductility synergy, Scr. Mater. 164 (2019) 30–35.
[60] Y.J. Liang, L. Wang, Y. Wen, B. Cheng, Q. Wu, T. Cao, Q. Xiao, Y. Xue, G. Sha, Y. Wang, Y. Ren, X. Li, L. Wang, F. Wang, H. Cai, High-content ductile coherent nanoprecipitates achieve ultrastrong high-entropy alloys, Nat. Commun. 9 (2018) 4063.
[61] Y. Ma, J.M. Hao, J.C. Jie, Q. Wang, C. Dong, Coherent precipitation and strengthening in a dual-phase AlNi2Co2Fe1.5Cr1.5 high-entropy alloy, Mater. Sci. Eng. A 764 (2019), 138241.
[62] F. He, Z.S. Yang, S.F. Liu, D. Chen, W.T. Lin, T. Yang, D.X. Wei, Z.J. Wang, J. C. Wang, J.J. Kai, Strain partitioning enables excellent tensile ductility in precipitated heterogeneous high-entropy alloys with gigapascal yield strength, Int. J. Plast. 144 (2021), 103022.
[63] A.M. Manzoni, S. Haas, J.M. Yu, H.M. Daoud, U. Glatzel, H. Aboulfadl, F. Mücklich, R. Duran, G. Schmitz, D.M. Többens, S. Matsumura, F. Vogel, N. Wanderka, Evolution of γ/γ' phases, their misfit and volume fractions in Al10Co25Cr8Fe15Ni36Ti6 compositionally complex alloy, Mater. Charact. 154 (2019) 363–376.
[64] X.L. Wu, Y.T. Zhu, Gradient and lamellar heterostructures for superior mechanical properties, MRS Bull. 46 (2021) 244–249.
[65] H.J. Gao, Y.G. Huang, W.D. Nix, J.W. Hutchinson, Mechanism-based strain gradient plasticity - I. theory, J. Mech. Phys. Solids. 47 (1999) 1239–1263.
[66] L.P. Kubin, A. Mortensen, Geometrically necessary dislocations and strain-gradient plasticity: a few critical issues, Scr. Mater. 48 (2003) 119–125.
[67] N. Hansen, Hall–Petch relation and boundary strengthening, Scr. Mater. 51 (2004) 801–806.
[68] H.M. Wen, T.D. Topping, D. Isheim, D.N. Seidman, E.J. Lavernia, Strengthening mechanisms in a high-strength bulk nanostructured Cu–Zn–Al alloy processed via cryomilling and spark plasma sintering, Acta Mater. 61 (2013) 2769–2782.
[69] K.K. Ma, H. Wen, T. Hu, T.D. Topping, D. Isheim, D.N. Seidman, E.J. Lavernia, J. M. Schoenung, Mechanical behavior and strengthening mechanisms in ultrafine grain precipitation-strengthened aluminum alloy, Acta Mater. 62 (2014) 141–155.
[70] D.N. Seidman, E.A. Marquis, D.C. Dunand, Precipitation strengthening at ambient and elevated temperatures of heat-treatable Al(Sc) alloys, Acta Mater. 50 (2002) 4021–4035.
[71] J.Y. He, H. Wang, H.L. Huang, X.D. Xu, M.W. Chen, Y. Wu, X.J. Liu, T.G. Nieh, K. An, Z.P. Lu, A precipitation-hardened high-entropy alloy with outstanding tensile properties, Acta Mater. 102 (2016) 187–196.
[72] N.Q. Vo, C.H. Liebscher, M.J.S. Rawlings, M. Asta, D.C. Dunand, Creep properties and microstructure of a precipitation-strengthened ferritic Fe–Al–Ni–Cr alloy, Acta Mater. 71 (2014) 89–99.
[73] Q.J. Li, H. Sheng, E. Ma, Strengthening in multi-principal element alloys with local-chemical-order roughened dislocation pathways, Nat. Commun. 10 (2019) 3563.
[74] R.P. Zhang, S.T. Zhao, J. Ding, Y. Chong, T. Jia, C. Ophus, M. Asta, R.O. Ritchie, A. M. Minor, Short-range order and its impact on the CrCoNi medium-entropy alloy, Nature. 581 (2020) 283–287.

[75] A. Fantin, G.O. Lepore, A.M. Manzoni, S. Kasatikov, T. Scherb, T. Huthwelker, F. d'Acapito, G. Schumacher, Short-range chemical order and local lattice distortion in a compositionally complex alloy, Acta Mater. 193 (2020) 329–337.
[76] W.R. Jian, Z.C. Xie, S.Z. Xu, Y.Q. Su, X.H. Yao, I.J. Beyerlein, Effects of lattice distortion and chemical short-range order on the mechanisms of deformation in medium entropy alloy CoCrNi, Acta Mater. 199 (2020) 352–369.
[77] Q.Q. Ding, Y. Zhang, X. Chen, X.Q. Fu, D. Chen, S.J. Chen, L. Gu, F. Wei, H.B. Bei, Y.F. Gao, M.R. Wen, J.X. Li, Z. Zhang, T. Zhu, R.O. Ritchie, Q. Yu, Tuning element distribution, structure and properties by composition in high-entropy alloys, Nature. 574 (2019) 223–227.
[78] X.F. Chen, Q. Wang, Z.Y. Cheng, M. Zhu, H. Zhou, P. Jiang, L.L. Zhou, Q.Q. Xue, F. P. Yuan, J. Zhu, X.L. Wu, E. Ma, Direct observation of chemical short-range order in a medium-entropy alloy, Nature. 592 (2021) 712–716.